Study of the physical properties of BiFeO3 films obtained by RF sputtering using a homemade target

Julio Cesar Leal-Zayas [a], Ramón Álvaro Vargas-Ortiz [a,*], Jorge Luis Almaral-Sánchez [a], Jose Miguel Mendivil-Escalante [a], Roberto Silva-González [b], Karla Mariela Moya-Canul [b], Jesús Iván Peña-Flores [b], José Martín Yáñez-Limón [b]

[a] Universidad Autónoma de Sinaloa, Fuente de Poseidón y Prol. Ángel Flores S/N., Los Mochis, Sinaloa C.P. 81223, Mexico
[b] Centro de Investigación y Estudios Avanzados del I.P.N. Unidad Querétaro, Libramiento Norponiente No. 2000, Fracc. Real de Juriquilla, Querétaro, Querétaro C.P. 76230, Mexico

ARTICLE INFO

ABSTRACT

Ferroelectric materials have attracted significant attention in recent decades because they can be used in various electronic devices. $BiFeO_3$ (BFO) has a perovskite-type ABO_3 structure with antiferromagnetic and ferroelectric properties and a band gap within the visible light range, making it a promising candidate for use in sensors and solar cells. In this study, $BiFeO_3$ thin films were grown by radio frequency (RF) sputtering using a homemade target and sintered at different times to evaluate the influence of sintering time on their physical properties. Its physical properties were evaluated using X-ray diffraction (XRD), scanning electron microscopy (SEM), and Raman spectroscopy. These results revealed that all films maintained a perovskite-like structure with rhombohedral and bismuth-rich secondary phases ($Bi_2O_{2.33}$). Atomic force microscopy (AFM) and piezoresponse force micrography (PFM) images depicted the impact of sintering time on surface roughness and ferroelectric domain reorientation. The optical properties, such as n, k, and the band gap of all samples, were obtained using reflection-transmission spectroscopy. The photoresponse under dark, visible and UV illumination were evaluated on BFO films grown over glass-FTO substrate.

© 2024 The Authors. Published by Elsevier España, S.L.U. on behalf of SECV. This is an open access article under the CC BY-NC-ND license (http://creativecommons.org/licenses/by-nc-nd/4.0/).

Estudio de las propiedades físicas de películas de BiFeO₃ obtenidas mediante erosión catódica por RF utilizando un blanco casero

R E S U M E N

Palabras clave:
Ferroeléctrico
Ferrita de bismuto
Erosión catódica
Tiempo de sinterización
Espectroscopía óptica
Fotocorriente

Los materiales ferroeléctricos han atraído gran atención en las últimas décadas porque pueden utilizarse en diversos dispositivos electrónicos. El BiFeO₃ (BFO) tiene una estructura ABO₃ de tipo perovskita con propiedades antiferromagnéticas y ferroeléctricas y una banda prohibida dentro del rango de luz visible, lo que lo convierte en un candidato prometedor para su uso en sensores y celdas solares. En este estudio, películas delgadas de BiFeO₃ crecieron mediante erosión catódica por radiofrecuencia utilizando un blanco casero y se sinterizaron durante diferentes tiempos para evaluar la influencia del tiempo de sinterización en sus propiedades físicas. Sus propiedades físicas se evaluaron mediante difracción de rayos X (XRD), microscopia electrónica de barrido (SEM) y espectroscopia Raman. Estos resultados revelaron que todas las películas mantenían una estructura del tipo perovskita ABO₃ con fase romboédrica y una fase secundaria rica en bismuto (Bi₂O₂.₃₃). Las imágenes de microscopia de fuerza atómica (AFM) y microscopia de fuerza de respuesta piezoeléctrica (PFM) mostraron el impacto del tiempo de sinterización en la rugosidad de la superficie y reorientación de dominios ferroeléctricos. Las propiedades ópticas, como n, k y la banda prohibida de todas las muestras, se obtuvieron mediante espectroscopia de reflexión-transmisión. La fotorrespuesta bajo iluminación visible, UV y sin iluminación (oscura) se evaluó en películas de BFO depositadas sobre sustrato de vidrio-FTO.

Introduction

Bismuth ferrite (BiFeO₃ or BFO) is a ferroelectric material with an ABO₃ perovskite-type structure that has attracted much attention in recent decades due to its high phase transition temperatures (Neel and Curie temperatures), which make it a very promising material due its antiferromagnetic and ferroelectric properties at room temperature, a high dielectric constant, and its band gap is within the visible light range [1]. However, there are some major drawbacks in the synthesis of this material: The difficulty of obtaining it free of secondary phases, the presence of a spin cycloid that blocks the magnetic response and the high leakage current, which makes it very difficult to fully exploit its hypothetical ferroelectric behavior at room temperature [2,3]. Even more, there are some contributions in which the ferroelectric response has only been observed in doped BFO thin films at liquid nitrogen temperature [4]. The crystalline structure of this material is strongly related to its piezoelectric, pyroelectric, and ferroelectric properties. Additionally, BFO is environmentally friendly because it does not contain lead (Pb). Therefore, it is a potential candidate for replacing lead-based materials in electronic devices, such as sensors, actuators, photodetectors, and photovoltaic devices. The properties of these materials depend on the synthesis parameters [5]. The effect of heat treatment on the physical properties of ferroelectric materials has been analyzed for different systems [3–6]. Ayala et al. reported a change in the band gap of BFO powders at different sintering times and temperatures (2.36 eV without heat treatment, 2.11 eV, and 2.19 eV at 500 °C for 8 h 50 min, and 600 °C for 10 h 30 min, respectively) [6]. The heat treatment effect on the stability and formation of secondary phases of BFO powders obtained by sol–gel at different temperatures has been studied, and it was observed that the sample treated at 450 °C showed more significant suppression of secondary phases than the rest of the samples [7]. BFO thin films via sol–gel were deposited and thermally treated at 450, 500, and 550 °C for 2 h. Structural parameters such as crystal size (15.2–41.2 nm), roughness (1.847–5.239 nm), and band gap (2.83–2.65 eV) were affected as the sintering temperature increased [8]. In sol–gel thin films, samples sintered at 300 °C were mostly composed of secondary phases, however, when treated at 600 °C the BiFeO₃ phase was observed along with the secondary phases [9]. The effect of sintering temperature on thin films deposited by RF sputtering has been studied [10–12]. BFO thin films deposited by RF sputtering and sintered at 500–700 °C showed that the BFO is mostly observed at 600 °C, with secondary phases such as Bi₂SiO₅ and Bi₂Fe₄O₉ present in all samples [10]. However, the influence of sintering time on the physical properties, such as structural, ferroelectric, and optical in BFO thin films deposited by RF sputtering has not been widely studied. In this study, BFO thin films were deposited on glass and FTO substrates by RF sputtering from a ceramic target synthetized in our laboratory, free of secondary phases. Subsequently, they were sintered ex situ in atmospheric conditions at 550 °C for 30, 45, and 60 min. The effect of sintering time at constant temperature on its structural, ferroelectric, optical, and photoresponse properties were studied.

Material and methods

BiFeO₃ thin films were deposited via RF cathodic erosion using a homemade ceramic target of 2 in diameter fabricated with a modified solid-state reaction route. To manufacture the tar-

get, high-purity oxide powders (Bi_2O_3, Sigma–Aldrich 99.9% and Fe_2O_3, Sigma–Aldrich 99%) were used in stoichiometric proportions with a 5% excess of Bi to mitigate its volatilization. These were ground using a SPEX/mixer mill 8000 for 1 hour and subsequently uniaxial pressed using a hydraulic press under a pressure of 93 MPa. The pressed powders were subjected to a thermal treatment consisting of calcination at 820 °C for 90 min and then sintered at 850 °C for 90 min at air atmosphere without a second grinding process.

The growth of the BFO films consists of 3 layers on commercial Corning glass and FTO substrates. This process is done to prevent the formation of superficial cracks in the films during sintering, improve the nucleation surface and achieve a thickness close to 200 nm [13]. The deposition time for the first layer was 10 min, the second layer was deposited for 30 min, and the third layer for 50 min, all layers were deposited at 2.47 W/cm^2 of power at room temperature. During the synthesis of films each layer was subjected to ex situ sintering in atmospheric conditions at 550 °C at a heating rate of 10 °C/min using different times of heat treatment.

The sintering times were 30, 45, and 60 min, labeled as BFO30, BFO45, and BFO60, respectively. Finally, graphite contacts of 700 μm of diameter using graphite paint were deposited on all films to study electrical properties. A Lindberg ISB furnace was used for sintering. The crystalline structure was determined by X-ray diffraction using a RIGAKU Dmax 2100 diffractometer with a CuK$_\alpha$ source ($\lambda = 1.5406$ Å). The measurement range was carried out at 20–80° in 2θ with a step of 0.02° and 0.4 s per step. Crystalline phase concentrations, lattice parameters, and crystallite size were determined by Rietveld refinements using MAUD software. The surface morphology of thin films was obtained via SEM using a Philips XL30 ESEM scanning electron microscope. Raman spectra were obtained using a Horiba Jobin Yvon, DilorII Microraman spectrometer with He–Ne laser excitation line with a wavelength of 632.8 nm. Atomic force microscopy was conducted using a Bruker Nanoscope IV Dimension 3100 atomic force microscope to assess roughness, and a conductive tip was used to obtain Piezoresponse Force Microscopy (PFM) images. The reflection and transmission spectra for the analysis of optical properties were obtained on a Film Tek 3000 UV-Vis spectrometer in a range of 300–850 nm. An Agilent 4255C semiconductor parameter analyzer was used to measure current vs voltage (*I–V*) curves in dark and illumination conditions, with UV lamp (365 nm) and visible illumination LED lamp (420–700 nm).

Results and discussion

X-ray analysis

Fig. 1a shows the X-ray diffraction pattern of the sintered ceramic target in the range of 20–80° in 2θ. All peaks matched the crystallographic PDF #71-2494, corresponding to $BiFeO_3$ with a perovskite-type rhombohedral R3c (161) structure without secondary phases. The absence of secondary phases in the target is attributed to the addition of 5% excess Bi in the synthesis stage. This element volatilizes easily at temperatures above 800 °C and $BiFeO_3$ is very susceptible to forming secondary phases due to excess or deficiencies of
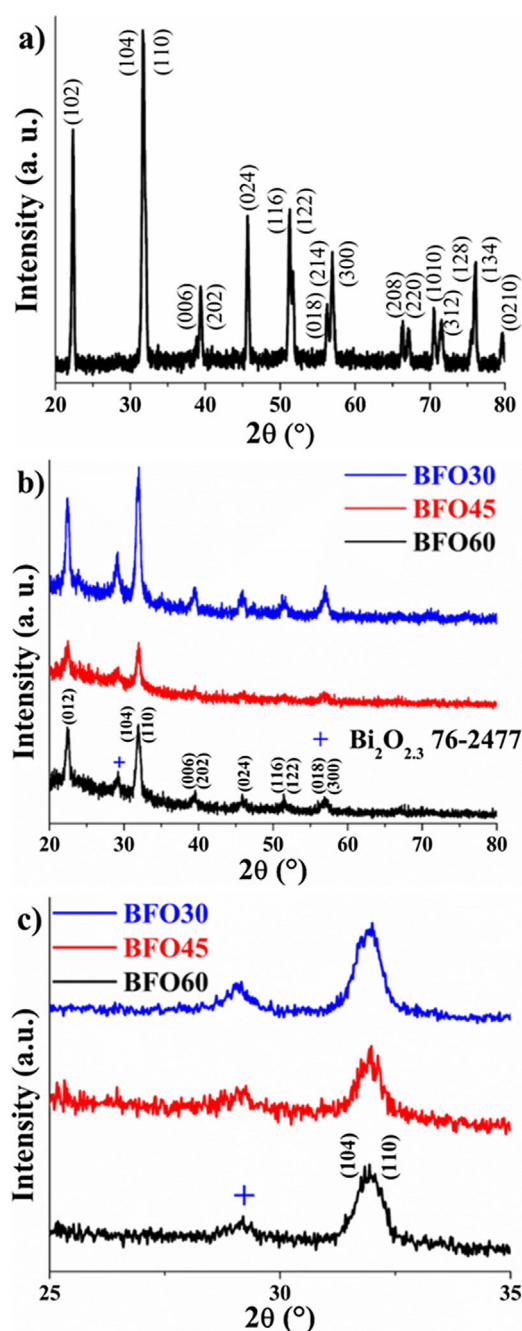

Fig. 1 – X-ray diffraction patterns of BiFeO₃ (a) home-made target and (b) and (c) thin films sintered at 550 °C for 30, 45 and 60 min.

Bi [14]. Therefore, the modified solid-state reaction route of the ceramic target to obtain a single perovskite phase without secondary phases was successful. Fig. 1b shows the diffraction patterns of $BiFeO_3$ thin films treated at different sintering times (BFO30, BFO45, and BFO60) on glass substrates in a range of 20–80° in 2θ. The diffraction peaks of all the samples matched with the PDF-86-1518 corresponding to $BiFeO_3$ with a perovskite-type structure with a rhombohedral phase. All films contain the secondary phase of $Bi_2O_{2.33}$ ("+" in the figure) around 29° in 2θ. The precipitation of Bi is attributed to

Table 1 – Refined structural parameters of BFO target and thin films using MAUD.

Samples	BFO target	BFO30	BFO45	BFO60
R3c (%)	100.0	76.8	50.4	76.8
a (Å)	5.5825	5.5855	5.5972	5.6102
c (Å)	13.8711	13.8510	13.7558	13.7382
CZ (nm)	20.64	14.74	14.10	12.52
$Bi_2O_{2.33}$ (%)	–	23.2	49.6	23.2
a (Å)	–	3.8436	3.8577	3.8301
c (Å)	–	35.8184	36.5993	35.8702
CZ (nm)	–	12.43	12.46	10.18
Σ	2.02	1.69	1.72	1.66

the pressure and temperature conditions used during deposition [15]. In Fig. 1c, an enlargement of the normalized principal peak between 25° and 35° in 2θ is shown, where it is evident that the position and shape of the peak remain unchanged. The above indicates that all samples possess the same rhombohedral R3c phase.

The lattice parameters were determined by Rietveld refinement using MAUD software (Table 1), revealing a subtle change in the "a" and "c" lattice parameters, increasing from 5.5855 Å to 5.6102 Å in "a" and decreasing from 13.8510 Å to 13.7382 Å in "c" as sintering time increased in the thin films. The crystal size decreased as the sintering time increased, from 14.74 nm to 12.52 nm. The percentage of the $Bi_2O_{2.33}$ secondary phase was quantified. These results indicate that samples sintered for 30 and 60 min have the lowest amount of this phase (23.2% in each sample). The BFO30 and BFO60 films exhibit higher intensity diffraction peaks than the BFO45 sample, this is due the high concentration of the secondary phase causes greater intensity in the peaks corresponding to this phase, which mitigates the intensity of the peaks corresponding to $BiFeO_3$. These non-sequential changes without clear trend are consistent with the thermal instability characteristic of $BiFeO_3$-based materials, where the structural, electrical, ferroelectric, and optical properties are influenced by heat treatments [10–13].

SEM

The surface micrographs (75,000×) of thin films of BFO at different sintering times (Fig. 2a, c, and e) show the granular morphology in each sample. Dense thin films are observed, with well-defined grains and no surface cracks. The morphology changes with the sintering time for each sample. The matrix average grain size (Fig. 3b, d, and f) is
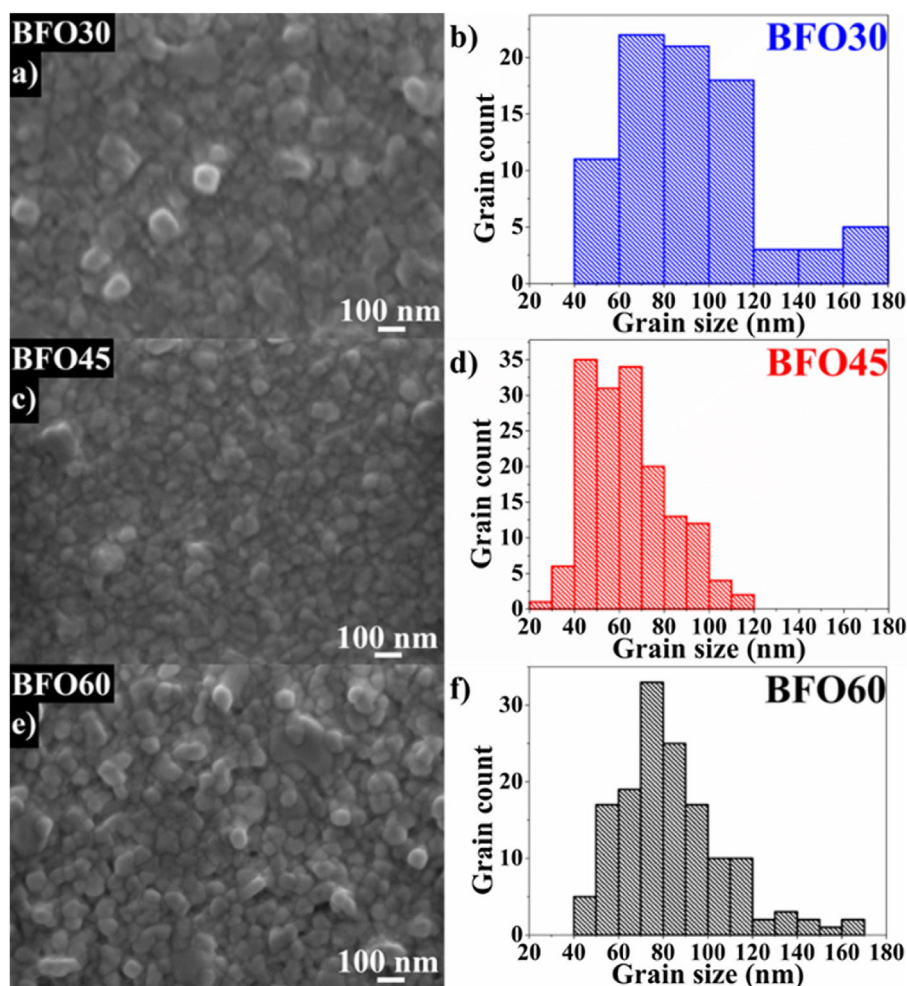

Fig. 2 – (a, c, and e) Surface scanning electron microscopy and (b, d, and f) grain size frequency histograms of BFO thin films sintered for 30, 45 and 60 min.
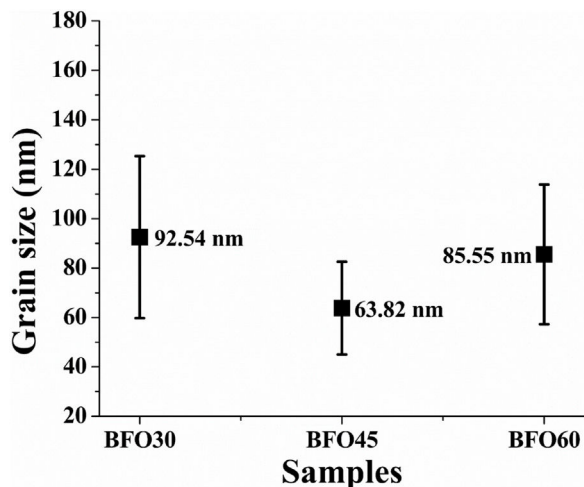
Fig. 3 – Grain size and standard deviation of BFO thin films sintered for 30, 45 and 60 min.

92.54 nm, 63.82 nm, and 85.55 nm, and the standard deviation is 32.78 nm, 18.77 nm, and 28.28 nm for BFO30, BFO45, and BFO60, respectively. A trend of grain size reduction was observed for all the films, with a notable drop in BFO45. Furthermore, larger grains with a brighter tone in all films correspond to agglomerations of bismuth oxide ($Bi_2O_{2.33}$), confirming the results obtained from X-ray patterns and the Rietveld analysis. The presence of secondary phases can influence the suppression of grain growth in ferroelectric materials [14,15]. In our case, the presence of a bismuth-rich phase ($Bi_2O_{2.33}$) leads to a reduction in grain size. The sample with the highest concentration of the secondary phase exhibits the smallest grain size (BFO45) [16,17].

Raman spectra

Fig. 4a shows the room temperature Raman spectra of $BiFeO_3$ thin films sintered at different times. Group theory predicts 13 active Raman modes for rhombohedral distorted BFO in the R3c symmetry, $\Gamma = 4A_1 + 9E$ [18]. 13 Raman modes for the sintered $BiFeO_3$ thin films at different times (BFO30, BFO45, and BFO60) were distinguished. In general, the A_{1-1}, A_{1-2}, A_{1-3}, and A_{1-4} modes (+) are distinguished at approximately 139 cm^{-1}, 167 cm^{-1}, 217 cm^{-1}, and 441 cm^{-1} respectively, along with 9 E modes (*) at around 75 cm^{-1}, 259 cm^{-1}, 266 cm^{-1}, 306 cm^{-1}, 343 cm^{-1}, 367 cm^{-1}, 463 cm^{-1}, 558 cm^{-1}, and 617 cm^{-1} (Fig. 4b). These modes were fitted according to studies of Kothari et al. of rhombohedral $BiFeO_3$ in the R3c symmetry [19]. It has been reported that the low-frequency modes are associated with the vibration of Bi—O bonds [20], and the high-frequency modes are attributed to Fe—O bonds. As the sintering time increases, the modes observed in the range from 217 cm^{-1} to 441 cm^{-1} increase in intensity and definition. This is clearly observed when comparing BFO30 with BFO45 and BFO60, where the modes A_{1-3}, E-2, E-3, E-4, E-5, E-6, and A_{1-4}. All of the above indicates structural distortions as time increases [21]. The $Bi_2O_{2.33}$ phase (#) appears as expected according to the results obtained through X-ray diffraction (DRX) and Rietveld analysis. In BFO45, two prominent peaks around 272 cm^{-1} and
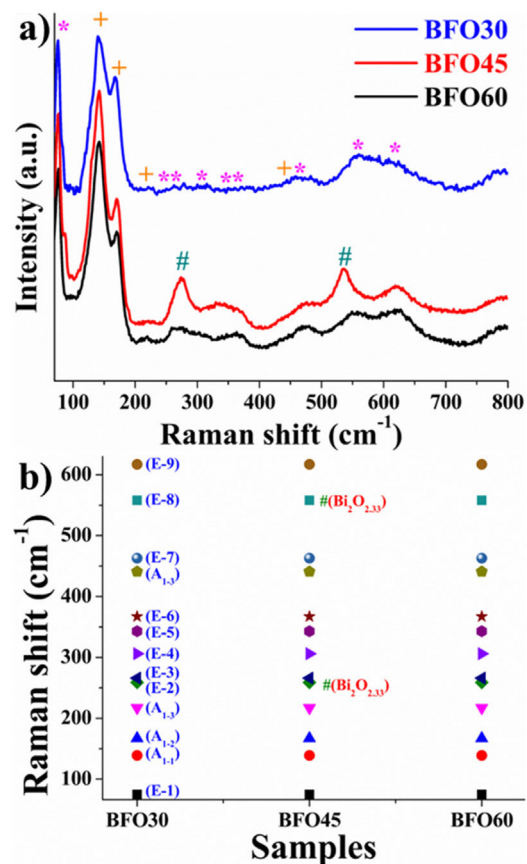

Fig. 4 – (a) Raman spectra and (b) modes of $BiFeO_3$ thin films sintered at different times.

534 cm^{-1} are observed, which corresponds to $Bi_2O_{2.33}$ and is not present in the other samples [21,22].

AFM

The atomic force microscopy images of BFO thin films at different sintering times show the topography of each sample (Fig. 5a–c). The roughness changes with sintering time: 20.3 ± 0.095 nm, 25.7 ± 0.080 nm, and 20.8 ± 0.072 nm for BFO30, BFO45, and BFO60, respectively. Some columnar-like growth is observed in all films; this is common in thin films of $BiFeO_3$ grown by RF sputtering [18–21,23], significantly impacting the roughness of thin films deposited by this technique. It has been reported that the deposition of bismuth oxide (Bi_2O_3) by RF sputtering can acquire the texture of nanotubes, so the high concentration of this secondary phase can promote columnar growth [24], which causes a difference in roughness due to the presence of different phases as seen in all samples. These results explain the observed roughness behavior (Fig. 5d), as the film with a higher concentration of bismuth oxide phase (BFO45) has a higher concentration of columns per unit area than those with a lower concentration of this phase (BFO30 and BFO60).

PFM

The structure of ferroelectric domains was studied by piezoresponse force microscopy (PFM), where out-of-plane phase
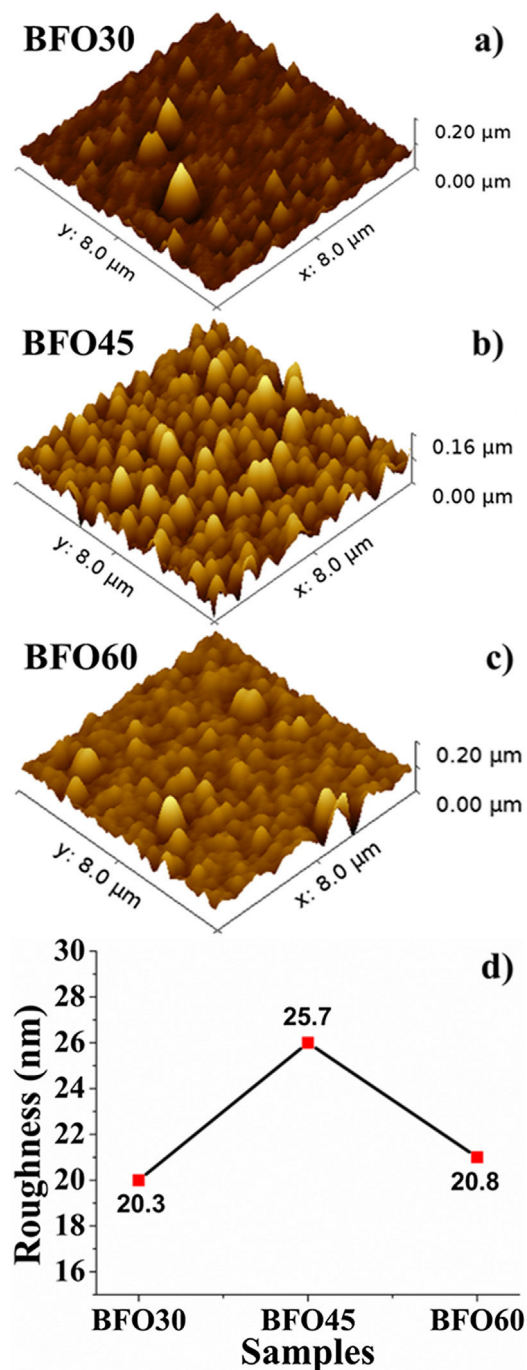
Fig. 5 – **(a–c) 3D surface atomic force micrographs and (d) roughness of thin films of BFO sintered for 30, 45, and 60 min.**

Fig. 6 – **Phase PFM images of BFO thin films sintered at different times.**

micrographs were obtained (Fig. 6a–c). The tone contrast is due to the difference in direction of the polarization vector, indicating a random polarization of ferroelectric domains despite the current leakage common in this material. This is unequivocal evidence of the presence of ferroelectric domains in all samples. The reorientation of ferroelectric domains in all samples of the $BiFeO_3$ system treated at different sintering times was achieved, as observed in the contrast difference due to changes in the direction of the polarization vector [25–27].
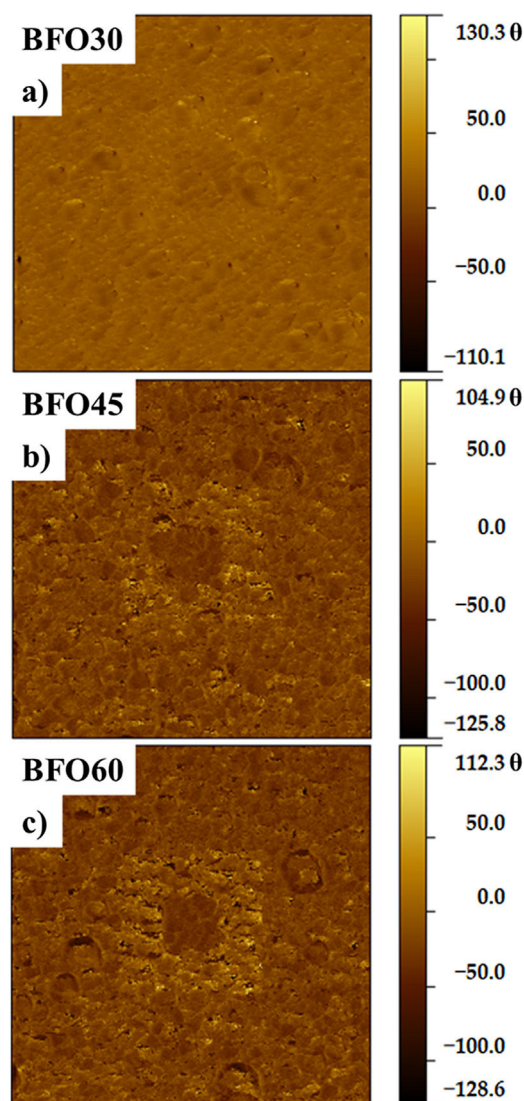
The ferroelectric domain polarization reversal was achieved by applying a voltage of $\pm 9\,V$ to areas of $3\,\mu m \times 3\,\mu m$ and $1\,\mu m \times 1\,\mu m$. The domain reorientation increased as the sintering time increased from 30 min to 60 min (Fig. 7). The above was determined based on the $\Delta\theta$ (Fig. 7 inset, Gwyddion V. 2.36 program) between the regions polarized at $+9\,V$ and $-9\,V$ [28]. All samples exhibit the ferroelectric characteristic of domain reorientation, where $\Delta\theta$ is strongly influenced by the sintering time.

Optical analysis

Fig. 8a displays the optical transmission and reflection spectra of thin $BiFeO_3$ thin film sintered for 60 min (dotted line) and its adjustment using a three-medium SCI model (continuous line) in FilmWizzard software. There is a low transmittance in the near-ultraviolet region of the spectrum. A sustained increase in transmittance is observed in the spectral range from 420 nm to 540 nm. The transmittance of the BFO60 film
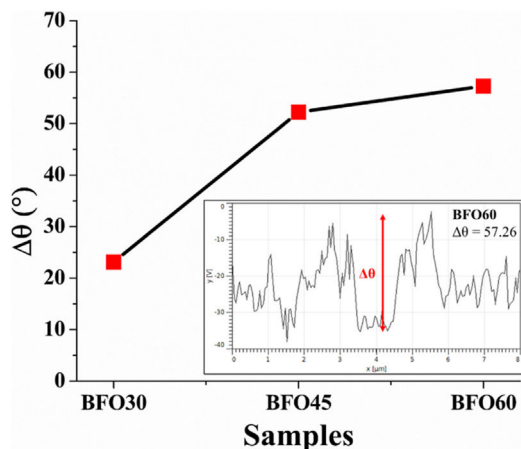
Fig. 7 – $\Delta\theta$ trend of different polarized regions of BFO thin films sintered at different times.

has a linear increase between 550 nm and 780 nm, reaching values close to 85%. In the near-infrared region, the transmittance increases with the sintering time. All samples refractive index (n) and extinction coefficient (k) are shown in Fig. 8b–d. Peaks of the refractive index (2.43–2.8) appear between 400 nm and 450 nm, which likely corresponds to a transition in the direct energy band gap in the visible light region. There is an increase in the extinction coefficient for samples BFO30 and BFO60 at lower wavelengths; this may indicate the effect that sintering time and the presence of secondary phases have on light absorption. Therefore, it is possible to modify the optical constants of this material thin films by selecting an appropriate sintering time, which may be necessary when designing optoelectronic devices. There are sharp drops from 266 nm to 600 nm in k, and beyond 600 nm is close to zero in all samples.

The thickness of all samples decreases as the sintering time increases. These were obtained by two methods: cross-sectional SEM images and UV–Vis Reflection-Transmission adjustment spectra. The thickness measured by a SEM image analyzer (Lince) was 191.5 ± 13.83 nm, 164.5 ± 14.19 nm, and 157.2 ± 12.35 nm for BFO30, BFO45, and BFO60, respectively. The thickness obtained by reflection-transmission adjustment spectra was 227 nm, 183 nm, and 112 nm for BFO30, BFO45, and BFO60, respectively. The difference in thickness values obtained by SEM and by reflection-transmission spectra analysis is because in SEM images the thickness is obtained through the analysis of the cross section of the thin films, while by reflection-transmission spectra analysis it is obtained from models considering several aspects such as roughness. However, in both it is possible to observe the same tendency of thickness reduction with increasing sintering time. The analysis of the absorption coefficient spectrum of the films reveals the contribution of different absorption processes. Fig. 9 shows strong absorption in the ultraviolet region of the spectrum as a result of excitations through the fundamental band gap. The absorption coefficient value increases with the sintering time and the decrease in thickness. The 550–850 nm region is the transparent area of the films regardless of their thickness. The
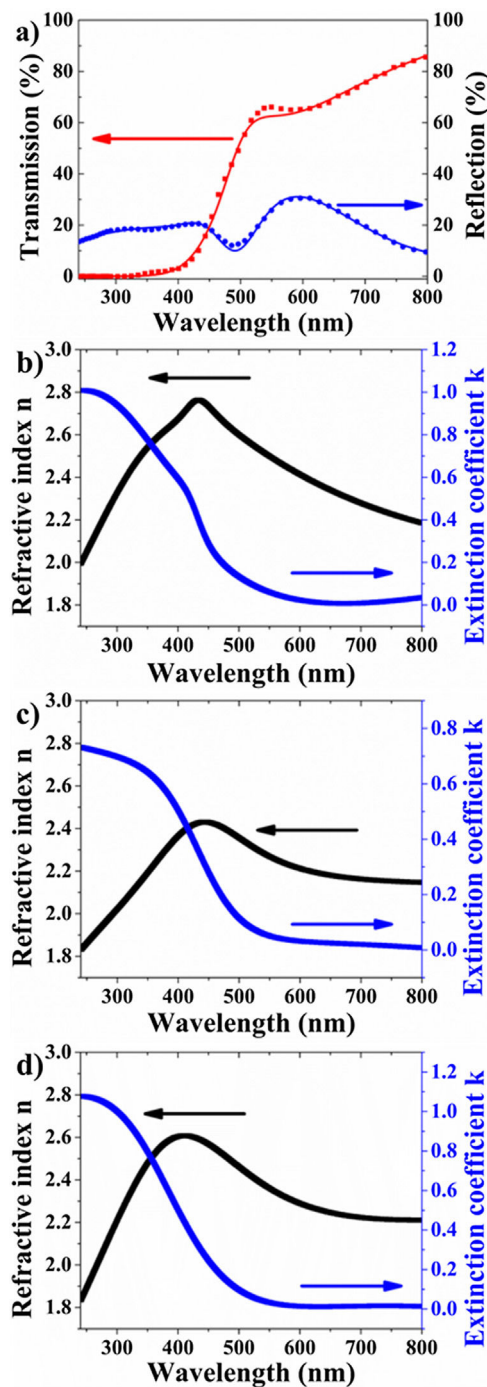

Fig. 8 – (a) Optical transmission and reflection spectra of BFO thin film for BFO60, n and k spectra of (b) BFO30, (c) BFO45 and (d) BFO60.

absorption coefficient $\alpha(\lambda)$ of all thin films was calculated by the Eq. (1) [29]:

$$\alpha(\lambda) = \frac{1}{d} ln\left(\frac{1}{T(\lambda)}\right),$$ (1)

where $T(\lambda)$ is the transmittance for a given wavelength λ and d is the film thickness.
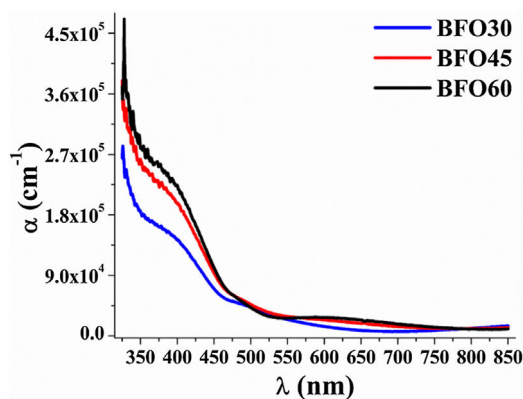
Fig. 9 – Absorption spectrum of BFO thin films sintered at different times in the 300–850 nm region.

The absorption coefficient analysis as a function of photon energy at the fundamental absorption edge allows the determination of the optical band gap and the type of electronic transition. The optical band gap of the samples (E_g) was estimated using the Tauc method for allowed direct transitions [30]. Fig. 10a–c shows that the band gap value for all samples was 2.74–2.75 eV. All films have a band gap within the visible spectrum, where the slight variations can be explained by discrete structural changes as is determined by Rietveld refinement. Thus, a Jahn–Teller type distortions in the Fe—O octahedron is observed via slight changes in E_g.

Photocurrent behavior

Fig. 11a–c shows the current density (J)–voltage (V) graphs at room temperature of BFO thin films sintered at 550 °C for 30, 45, and 60 min (BFO30, BFO45, and BFO60, respectively). The effect of sintering time, as well as the presence of the $Bi_2O_{2.33}$ phase, is observed. The presence of secondary phases yields a high concentration of oxygen vacancies, which promotes charge carriers [31]. A diode-like effect was obtained in samples BFO30 and BFO60 due to the Schottky barrier formed at the interface of the BFO film and the FTO substrate; this is a typical behavior in $BiFeO_3$ based thin films [32,33]. The current density (J) decreases as sintering time increases, as seen for the sample BFO30 at 1 V (2.97×10^{-4} A/cm^2) and BFO60 at 1 V (2.02×10^{-5} A/cm^2). It is also shown in Fig. 11 the current behavior under no illumination (Dark or D), visible light (Vis), and visible light with ultraviolet light (Vis + UV) using two lamps on all BFO films. All samples exhibit a photoconductive behavior when subjected to both types of light (Vis and Vis + UV). This is due to the generation of charge carriers induced by illumination with an energy higher than the material's band gap. The generation of charge carriers through excitation with light is possible in BFO base films and, therefore, induces photocurrent [34]. All this is evidence that sintering time greatly affects the electrical and photocurrent properties of BFO thin films.

The results show that the films obtained by sputtering with different sintering times in ambient conditions, using a homemade ceramic target synthesized in our laboratory free of secondary phases, allow us to obtain films with the
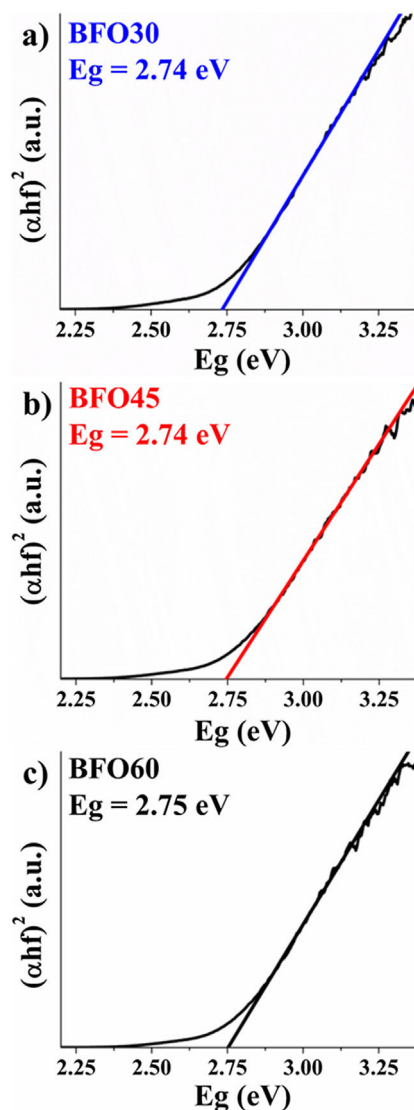

Fig. 10 – Tauc plots of BFO thin films sintered at different times.

rhombohedral phase of BFO starting from 30 min of thermal treatment. However, the secondary phase $Bi_2O_{2.3}$ appears in all thin films. The samples have a wide grain size distribution, with mean values close to 85 nm and a standard deviation close to 25 nm, such that the average grain size is within the error bar for all treatment times. Due to the columnar nature of grain growth through sputtering, roughness around 20 nm is obtained. However, the results show apparent effects due to the sintering time, among which is densification, as seen in the reduction in thickness of the films. There is a tendency to decrease the roughness, and a better contrast is also observed in the reorientation of induced ferroelectric domains for the sample with longer sintering time. The absorption coefficient shows an increasing trend with sintering time. In the J–V curves, it can be observed that there is a decrease in the current density for the sample with longer thermal treatment time, which may be due to a decrease in the concentration of defects, promoting the ferroelectric properties and therefore
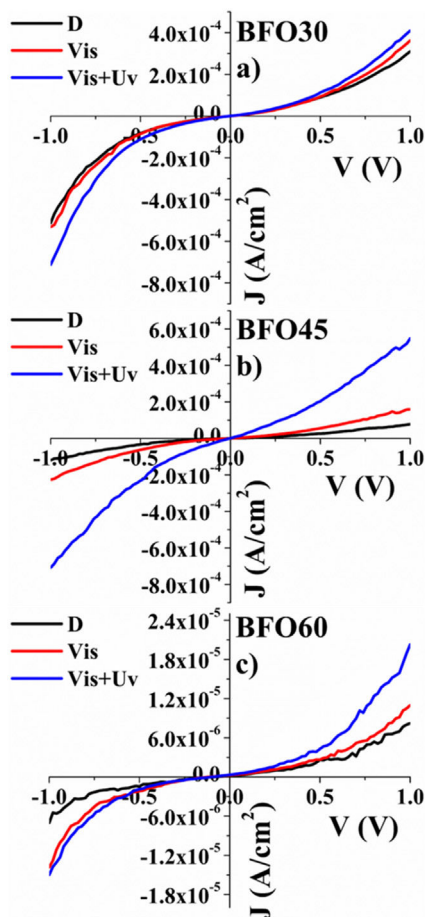
Fig. 11 – I–V graphs of BFO thin films sintered at 550°C for 30, 45 and 60 min.

improving the contrast observed in the induced ferroelectric domains. To improve the ferroelectric properties of BFO films, a synthesis and post-processing method that eliminates or appreciably reduces the presence of the secondary phase is desirable. In future work, this problem will be addressed by implementing control of the substrate temperature inside the chamber of growth. Alternatively, in the post-processing method, the films can be treated in an inert atmosphere or subjected to rapid thermal processing to avoid the formation of the secondary phase.

Conclusions

$BiFeO_3$ thin films were deposited using a home-made target free of secondary phases, by RF sputtering and ex situ sintered at different times. A bismuth-rich secondary phase, changes in lattice parameters, phase percentage and crystallite size were identified in all films as increasing sintering time. The grain size was reduced from 92.54 nm to 85.55 nm for BFO30 and BFO60, respectively. Furthermore, grain size suppression was promoted by the presence of $B_2O_{2.33}$ as seen in BFO45. Raman spectroscopy allows us to corroborate the structural changes and the presence of the secondary phase as sintering time increases. The presence of the secondary phase propor-

tionally influences the roughness of all films. Reorientation and observation of ferroelectric domains through PFM in all samples were performed. The $\Delta\theta$ increased as sintering time increased and thickness decreased. The elucidation of n and k spectra allows us to determine the effect of sintering time on the optical properties of BFO thin films. The band gap remained between 2.74 eV and 2.75 eV because the structural changes did not sufficiently affect the Jahn–Teller octahedron in the Fe—O octahedron. A diode-like effect was observed in BFO30 and BFO60 films, and a photocurrent was observed in all samples. Sintering time has various effects on the physical properties of $BiFeO_3$ thin films, so it is essential to consider this factor for an adequate design of optoelectronic devices composed of this material.

Acknowledgments

REFERENCES

[1] C. Gumiel, D.G. Calatayud, Thin film processing of multiferroic $BiFeO_3$: from sophistication to simplicity. A review, Bol. Soc. Esp. Ceram. Vidr. 61 (6) (2021) 708–732, http://dx.doi.org/10.1016/j.bsecv.2021.08.002.

[2] C. Gumiel, et al., Combination of structural and microstructural effects in the multiferroic response of Nd and Ti co-doped $BiFeO_3$ bulk ceramics, Ceram. Int. 45 (5) (2019) 5276–5283, http://dx.doi.org/10.1016/j.ceramint.2018.11.225.

[3] C. Gumiel, et al., Suppressing the non-switching contribution in $BiFeO_3$–$Bi_4Ti_3O_{12}$ based thin film composites to produce room-temperature multiferroic behavior, J. Eur. Ceram. Soc. 42 (13) (2022) 5615–5623, http://dx.doi.org/10.1016/j.jeurceramsoc.2022.06.004.

[4] C. Gumiel, et al., Nanostructure stabilization by low-temperature dopant pinning in multiferroic $BiFeO_3$-based thin films produced by aqueous chemical solution deposition, J. Mater. Chem. C 8 (12) (2020) 4234–4245, http://dx.doi.org/10.1039/c9tc05912a.

[5] J. Silva, A. Reyes, H. Esparza, H. Camacho, L. Fuentes, $BiFeO_3$: a review on synthesis, doping and crystal structure, Integr. Ferroelectr. 126 (1) (2011) 47–59, http://dx.doi.org/10.1080/10584587.2011.574986.

[6] Z.B. Ayala, J.J. Peñalva, C.R. Eyzaguirre, H. Loro, A. Lazo, Y.J.M. Hernández, Study of the optical properties of $BiFeO_3$ under different heat treatment temperatures, J. Phys. Conf. Ser. 2372 (1) (2022) 012005, http://dx.doi.org/10.1088/1742-6596/2372/1/012005.

[7] R.L. Palomino-Resendiz, A.M. Bolarín-Miró, F. Pedro-García, F. Sánchez-De Jesús, J.P. Espinós-Manzorro, C.A.

Cortés-Escobedo, Analysis of the effect of cationic ratio Bi^{3+}/Fe^{3+} on the magnetic and multiferroic properties of $BiFeO_3$ nanoparticles synthesized using a sonochemical-assisted method, Ceram. Int. 48 (10) (2022) 14746–14753, http://dx.doi.org/10.1016/j.ceramint.2022.02.011.

[8] A. Deepak Sharma, H. Basantakumar Sharma, Influence of sintering temperature on structural, morphological and optical properties of nanocrystalline bismuth ferrite thin films via sol–gel processing, IOP Conf. Ser. Mater. Sci. Eng. 1219 (1) (2022) 012052, http://dx.doi.org/10.1088/1757-899x/1219/1/012052.

[9] T. Dash, P. Sahoo, N. Mohanty, R. Kishore Mishra, B.B. Palei, Effect of low sintering temperature on the synthesis of $BiFeO_3$, Mater. Today Proc. 43 (2020) 220–223, http://dx.doi.org/10.1016/j.matpr.2020.11.642.

[10] N. Siadou, I. Panagiotopoulos, N. Kourkoumelis, T. Bakas, K. Brintakis, A. Lappas, Electric and magnetic properties of sputter deposited $BiFeO_3$ films, Adv. Mater. Sci. Eng. 2013 (i) (2013), http://dx.doi.org/10.1155/2013/857465.

[11] J.N. Ding, M.J. Chen, J.H. Qiu, N.Y. Yuan, Photovoltaic properties of ferroelectric solar cells based on polycrystalline $BiFeO_3$ films sputtered on indium tin oxide substrates, Sci. China Phys. Mech. Astron. 58 (3) (2015) 1–6, http://dx.doi.org/10.1007/s11433-014-5552-8.

[12] P. Couture, et al., Nanocrystalline multiferroic $BiFeO_3$ thin films made by room temperature sputtering and thermal annealing, and formation of an iron oxide-induced exchange bias, J. Alloys Compd. 695 (2017) 3061–3068, http://dx.doi.org/10.1016/j.jallcom.2016.11.344.

[13] O. García-Zaldívar, M.C. Rodríguez-Aranda, S. Díaz-Castañón, F. Calderón-Piñar, F.J. Flores-Ruiz, J.M. Yáñez-Limón, Influence of deposition procedure on the properties of multiferroic $BiFeO_3$-based thin films deposited by radio frequency sputtering, Appl. Phys. A Mater. Sci. Process. 124 (12) (2018), http://dx.doi.org/10.1007/s00339-018-2216-y.

[14] X. Wu, L. Yao, S. Yang, Y. Zhang, Enhanced ferroelectricity and band gap engineering of $(1-x)BiFeO_3-xSrTiO_3$ thin films, J. Sol–Gel Sci. Technol. 83 (3) (2017) 653–659, http://dx.doi.org/10.1007/s10971-017-4441-9.

[15] H. Béa, et al., Influence of parasitic phases on the properties of $BiFeO_3$ epitaxial thin films, Appl. Phys. Lett. 87 (7) (2005) 072508, http://dx.doi.org/10.1063/1.2009808.

[16] T.T. Carvalho, P.B. Tavares, Synthesis and thermodynamic stability of multiferroic $BiFeO_3$, Mater. Lett. 62 (24) (2008) 3984–3986, http://dx.doi.org/10.1016/j.matlet.2008.05.051.

[17] X. Deng, X. Liu, W. Cai, C. Fu, J. Huang, The influence of sintering temperature on the microstructure and electrical properties of $BiFeO_3$ ceramics, Key Eng. Mater. 602–603 (2014) 942–946, http://dx.doi.org/10.4028/www.scientific.net/KEM.602-603.942.

[18] H. Fukumura, et al., Observation of phonons in multiferroic $BiFeO_3$ single crystals by Raman scattering, J. Phys. Condens. Matter 19 (36) (2007) 365224, http://dx.doi.org/10.1088/0953-8984/19/36/365224.

[19] D. Kothari, V. Raghavendra Reddy, V.G. Sathe, A. Gupta, A. Banerjee, A.M. Awasthi, Raman scattering study of polycrystalline magnetoelectric $BiFeO_3$, J. Magn. Magn. Mater. 320 (3–4) (2008) 548–552, http://dx.doi.org/10.1016/j.jmmm.2007.07.016.

[20] W. Liu, G. Tan, X. Xue, G. Dong, H. Ren, A. Xia, Phase transition and enhanced multiferroic properties of (Sm, Mn and Cr) co-doped $BiFeO_3$ thin films, Ceram. Int. 40 (8 Part A) (2014) 12179–12185, http://dx.doi.org/10.1016/j.ceramint.2014.04.058.

[21] G. Dong, G. Tan, Y. Luo, W. Liu, H. Ren, A. Xia, Optimization of the multiferroic $BiFeO_3$ thin films by divalent ion (Mn, Ni) co-doping at B-sites, Mater. Lett. 118 (2014) 31–33, http://dx.doi.org/10.1016/j.matlet.2013.12.039.

[22] O. Depablos-Rivera, A. Martínez, S.E. Rodil, Interpretation of the Raman spectra of bismuth oxide thin films presenting different crystallographic phases, J. Alloys Compd. 853 (2021) 157245, http://dx.doi.org/10.1016/j.jallcom.2020.157245.

[23] M. Valant, A.K. Axelsson, N. Alford, Peculiarities of a solid-state synthesis of multiferroic polycrystalline $BiFeO_3$, Chem. Mater. 19 (22) (2007) 5431–5436, http://dx.doi.org/10.1021/cm071730+.

[24] B. Sirota, J. Reyes-Cuellar, P. Kohli, L. Wang, M.E. McCarroll, S.M. Aouadi, Bismuth oxide photocatalytic nanostructures produced by magnetron sputtering deposition, Thin Solid Films 520 (19) (2012) 6118–6123, http://dx.doi.org/10.1016/j.tsf.2012.06.001.

[25] M. Vila, C. Díaz-Guerra, J. Piqueras, Luminescence and Raman study of α-Bi_2O_3 ceramics, Mater. Chem. Phys. 133 (1) (2012) 559–564, http://dx.doi.org/10.1016/j.matchemphys.2012.01.088.

[26] Y.T. Liu, S.Y. Chen, H.Y. Lee, Characteristics of highly oriented $BiFeO_3$ thin films on a $LaNiO_3$-coated Si substrate by RF sputtering, Thin Solid Films 518 (24) (2010) 7412–7415, http://dx.doi.org/10.1016/j.tsf.2010.05.003.

[27] C. Ostos, O. Raymond, N. Suarez-Almodovar, D. Bueno-Baqués, L. Mestres, J.M. Siqueiros, Highly textured Sr, Nb co-doped $BiFeO_3$ thin films grown on $SrRuO_3$/Si substrates by rf-sputtering, J. Appl. Phys. 110 (2) (2011) 024114, http://dx.doi.org/10.1063/1.3610428.

[28] M. Khodaei, et al., Ferroelectric and piezoelectric behavior of (111)-oriented $Pb(Zr_xTi_{1-x})O_3$ thin films on cobalt ferrite nano-seed layered Pt(111)/Si substrate, J. Mater. Sci. Mater. Electron. 25 (4) (2014) 1696–1702, http://dx.doi.org/10.1007/s10854-014-1785-6.

[29] D. Dwibedy, A.K. Sahoo, M.R. Panigrahi, Structural, microstructural and optical properties of perovskite $CCNb_xTi_{1-x}O$ ($x = 0.02$) thin film explored for photovoltaic applications, Optik (Stuttg.) 243 (October 2021) (2021) 167496, http://dx.doi.org/10.1016/j.ijleo.2021.167496.

[30] X.L. Liang, J.Q. Dai, Prominent ferroelectric properties in Mn-doped $BiFeO_3$ spin-coated thin films, J. Alloys Compd. 886 (2021) 161168, http://dx.doi.org/10.1016/j.jallcom.2021.161168.

[31] K. Laurent, G.Y. Wang, S. Tusseau-Nenez, Y. Leprince-Wang, Structure and conductivity studies of electrodeposited δ-Bi_2O_3, Solid State Ionics 178 (33–34) (2008) 1735–1739, http://dx.doi.org/10.1016/j.ssi.2007.11.013.

[32] J.J. Enriquez-Flores, C.I. Gervacio-Arciniega, F.J. Flores-Ruiz, D. Cardona, E. Camps, J. Muñoz-Saldaña, F.J. Espinoza-Beltrán, Piezoresponse force microscopy studies of pc-$BiFeO_3$ thin films produced by the simultaneous laser ablation of Bi and FeO_3, Mater. Res. Soc. Symp. Proc. 1477 (2012) 61–66, http://dx.doi.org/10.1557/opl.2012.

[33] M.P. Cruz, et al., Piezoelectric and ferroelectric response enhancement in multiferroic $YCrO_3$ films by reduction in thickness, Mater. Lett. 114 (2014) 148–151, http://dx.doi.org/10.1016/j.matlet.2013.10.009.

[34] B. Liu, Z. Peng, J. Ma, J. Wang, Q. Zhao, Y. Wang, Enhanced photovoltaic effect of polycrystalline $BiFeO_3$ film, Phys. Status Solidi Appl. Mater. Sci. 210 (4) (2013) 819–822, http://dx.doi.org/10.1002/pssa.201228789.